

A Regulation-Free Sub-0.5-V 16-/24-MHz Crystal Oscillator With 14.2-nJ Startup Energy and 31.8- μ W Steady-State Power

Ka-Meng Lei, *Member, IEEE*, Pui-In Mak^{ID}, *Senior Member, IEEE*, Man-Kay Law^{ID}, *Senior Member, IEEE*, and Rui P. Martins^{ID}, *Fellow, IEEE*

Abstract—This paper reports a regulation-free sub-0.5-V crystal oscillator (XO). The XO specifically designed for Bluetooth low-energy (BLE) radios aims for direct-powering by the harvested energy. To secure its performance against process, voltage, and temperature (PVT) variations, while reducing its startup time and energy, we propose a dual-mode g_m scheme and a scalable self-reference chirp injection (SSCI) technique. The former employs an inductive multistage g_m to mitigate the crystal's stray capacitance during the startup, but a single-stage g_m in the steady state to preserve the phase noise (PN). For the latter (SSCI), we generate a scalable chirping sequence to kick-start the XO, avoiding trimming of the auxiliary oscillator. The XO fabricated in 65-nm CMOS is measured with two common crystals (16/24 MHz) over a 0.3-to-0.5-V supply. At 24 MHz and 0.35 V, the startup time and energy of the XO are 400 μ s and 14.2 nJ, respectively, while showing a steady-state power of 31.8 μ W and a PN of -134 dBc/Hz at 1-kHz offset. The frequency stability is 14.1 ppm against temperature (-40 °C– 90 °C) and 17.9 ppm against voltage (0.3–0.5 V), both conform to the BLE standard (± 50 ppm) with adequate margin.

Index Terms—Bluetooth low-energy (BLE), chirping, CMOS, crystal oscillator (XO), duty-cycling, energy harvesting (EH), fast startup, Internet-of-Things (IoT), ultralow power (ULP), ultralow voltage (ULV).

Manuscript received March 10, 2018; revised May 13, 2018; accepted June 12, 2018. Date of publication July 4, 2018; date of current version August 27, 2018. This paper was approved by Associate Editor Andrea Baschiroto. This work was supported in part by the Macau Science and Technology Development Fund—SKL Fund and in part by the University of Macau under Grant MYRG2017-00223-AMSV. (*Corresponding author: Pui-In Mak.*)

K.-M. Lei is with the State Key Laboratory of Analog and Mixed Signal VLSI, University of Macau, Macau 999078, China, and also with Harvard University, Cambridge, MA 02138 USA.

P.-I. Mak is with the State Key Laboratory of Analog and Mixed-Signal VLSI, University of Macau, Macau 999078, China, and also with the Department of Electrical and Computer Engineering, Faculty of Science and Technology, University of Macau, Macau 999078, China (e-mail: pimak@umac.mo).

M.-K. Law is with the State Key Laboratory of Analog and Mixed Signal VLSI, University of Macau, Macau 999078, China.

R. P. Martins is with the State Key Laboratory of Analog and Mixed-Signal VLSI, University of Macau, Macau 999078, China, and also with the Department of Electrical and Computer Engineering, Faculty of Science and Technology, University of Macau, Macau 999078, China, on leave from the Instituto Superior Técnico, Universidade de Lisbon, 1049-001 Lisbon, Portugal.

Color versions of one or more of the figures in this paper are available online at <http://ieeexplore.ieee.org>.

Digital Object Identifier 10.1109/JSSC.2018.2849012

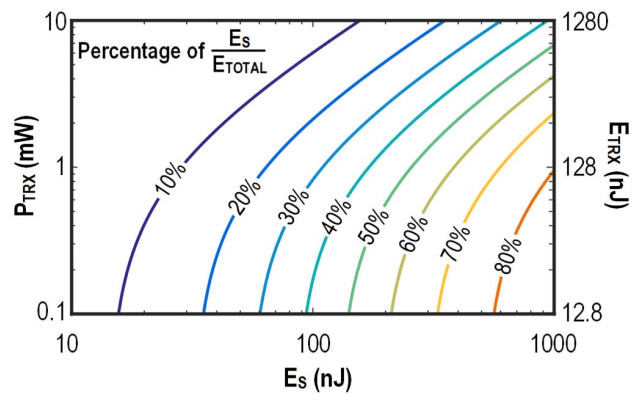


Fig. 1. Percentage of energy consumed during the startup of the XO over the total energy $E_{TOTAL} = P_{TRX} \times T_{ON} + P_{SLEEP} \times T_{OFF} + E_S$. P_{SLEEP} (assumed 1 μ W here, as approximated from [7]) is the sleep power, T_{ON} (128 μ s) and T_{OFF} (128 ms) are the assumed active time and sleep time of the TRX, respectively.

I. INTRODUCTION

ULTRALOW-POWER (ULP) wireless radios are the cornerstone of a wide variety of Internet-of-Things (IoT) applications. In particular, for the environmental monitoring, the ULP radios should operate under intermittent operation [1] to further reduce the data handling while prolonging the battery lifetime. Each ULP radio requires a stable reference for frequency synthesis at RF. The crystal oscillator (XO) is a reliable solution, but without the startup aid, it can take a few milliseconds for the XO to settle into the steady state [2]–[5] due to the high quality factor of the crystal ($\sim 10^5$). Its startup time (t_s) dominates the “ON” latency of the radio, and its startup energy (E_S) can significantly degrade the effectiveness of duty cycling. As depicted in Fig. 1, if the active energy (E_{TRX}) of a transceiver (TRX) is 1280 nJ (ON-time of 128 μ s [6] and active power of 10 mW [7]), the percentage of energy spent for starting the XO in every working cycle is $\sim 42\%$ for E_S of 1000 nJ for conventional XO and a duty cycle of 0.1%. Such a percentage is going up since recent TRXs have managed to lower their active power (P_{TRX}) by proper circuit techniques [8]–[10]. In this regard, it is essential to reduce E_S for the ULP radios to save energy by duty cycling. Recent efforts in both academia

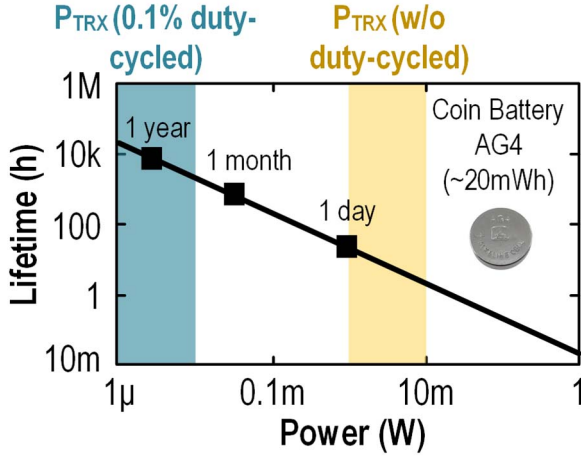


Fig. 2. Estimated lifetime of a commercial coin battery AG4 versus P_{TRX} , which can be expressed as: battery capacity/ $(P_{TRX} \times \text{active duty cycle})$.

and industry succeeded in shortening t_s and E_S of the XO [6], [7], [11]–[16].

On the other hand, long-term sustainability of wireless sensor nodes is another critical perspective of IoT deployment. For battery-powered ULP radios, the effort of battery replacement is largely labor-intensive. Even with a 0.1% active cycle, and a P_{TRX} of 2.3 mW, the lifetime of a ULP radio can hardly exceed a year under a coin-size battery (Fig. 2). For the prospect of one trillion IoT devices in the years to come, it implies 2.7 billion of batteries replacement daily, being a tremendous effort and unsustainable to the environment. To this end, energy harvesting (EH) offers the outlook for perpetual operation [17]–[19] of the ULP radios, while eliminating the cost and volume limit of the battery. Thermoelectric ($10\text{--}1000 \mu\text{W}/\text{cm}^2$) and photovoltaic (indoor: $10\text{--}100 \mu\text{W}/\text{cm}^2$) are promising ambient sources, but their sub-0.5-V outputs [17] are too low for typical circuit solutions, and can vary (although slowly) with the environmental factors (e.g., temperature or light intensity). These facts motivate a new paradigm of analog and RF circuits that can survive against an inconstant sub-0.5-V supply voltage (V_{DD}), eliminating the cost and loss of interim dc–dc converters and regulators.

This paper reports a regulation-free sub-0.5-V XO according to the system aspect of the EH Bluetooth low-energy (BLE) radios described in [20]–[23]. Unlike the existing fast-startup XOs that are based on standard or I/O voltages to power-up their inverter-like or active-load amplifiers [6], [11]–[14], our proposed XO is ultralow-voltage (ULV)-enabled by using single-/multistage resistive-load amplifiers. This circumvents from the ineluctable voltage headroom limit, rendering it compatible with the ULV application. Specifically, we propose a dual-mode g_m scheme and a scalable self-reference chirp injection (SSCI) technique for the XO to surmount the operating challenges in both startup and steady state (Fig. 3). The reported XO includes load capacitors of 6 pF and suits common commercially available crystals. Yet the technique can also be applied to crystals with different load capacitances.

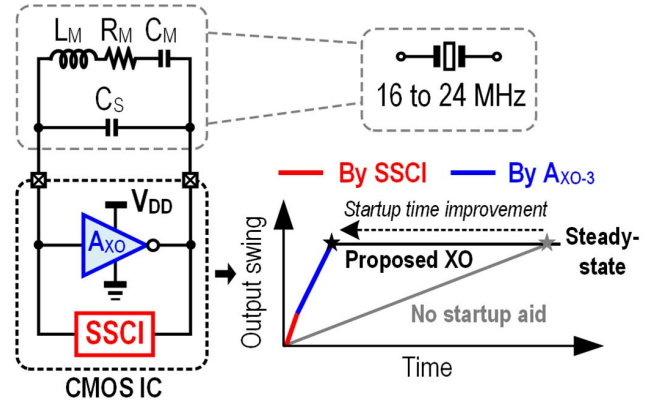


Fig. 3. Overview of the proposed XO and illustration of t_s improvement by two techniques: SSCI and inductive three-stage g_m . L_M , C_M , and R_M are the modeled inductance, capacitance, and resistance of the crystal, respectively, whereas C_S is the crystal's stray capacitance.

This paper is expanded from [24], with additional details and measurement results.

After the introduction, Section II details the proposed dual-mode g_m scheme and SSCI. Section III presents the transistor-level design of the sub-0.5-V XO. Section IV summarizes the experimental results, and finally, Section V draws conclusions.

II. FAST-STARTUP XO USING DUAL-MODE G_m SCHEME AND SSCI

For a crystal's resonant frequency (f_m) at tens of megahertz, its t_s (milliseconds) dominates the “ON” latency of a duty-cycled radio, raising the average power consumption. As well, for energy-limited EH sources, the startup energy (E_S) of the XO is crucial as it may demand a large instant current from the EH source or reservoir. Recent XOs [6], [11]–[15] have succeeded in reducing both t_s and E_S . Herein, we propose two techniques: dual-mode g_m and SSCI, for balancing the XO performances in both startup (i.e., t_s and E_S) and steady state [i.e., power consumption and phase noise (PN)]. The envelope of the XO during the startup at time t is

$$A_{\text{env}}(t) = A_i \cdot e^{\frac{R_N - R_M}{2L_M} t} \quad (1)$$

where A_i is the initial amplitude and R_N is the negative resistance of the overall impedance viewed from the crystal core (details in Section II-B). L_M and R_M are the motional inductance and resistance of the crystal, respectively. The aim of SSCI is to increase A_i instantly after enabling the XO, while the dual-mode g_m allows a boosted R_N afterward. They together bring down t_s without momentarily raising the startup power, culminating in a lower E_S and a relaxed power-source design, with details presented in the following.

A. Scalable Self-Reference Chirp Injection

Signal injection to the XO can bring down t_s if the injection frequency is close to f_m of the crystal [12]. Instead of waiting for the XO to build up its oscillation amplitude, an auxiliary oscillator (AO) can be used to excite the crystal. Yet, due to the high-Q nature of the crystal, such signal injection is only

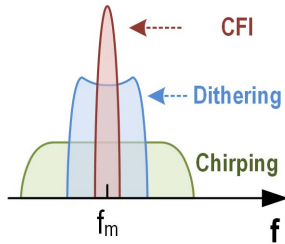


Fig. 4. General illustration of different signal-injection techniques in the frequency domain. Assuming the total power of each injection signal is similar, the crystal absorbs more power from CFI than CI since the CI spectrum spreads over a broader band.

effective if its frequency does not deviate by $>0.5\%$ from f_m [6]. Several signal-injection techniques for kick-starting the XO have been reported. They can be categorized into three groups: constant frequency injection (CFI) [11], [14], [15], dithering injection [6], and chirp injection (CI) [12].

CFI injects a clock signal into the crystal with a constant frequency close to f_m , as illustrated in the frequency domain (Fig. 4). With a constant frequency and narrow bandwidth (e.g., full-width at half-maximum of the $7.7\text{-}\mu\text{s}$ pulse in [14]: 156 kHz), a clock frequency precisely matching f_m is essential to excite the crystal. This involves calibration as well as a delicate design for the AO which will be challenging in a sub- 0.5-V design. As an example, the XO in [14] achieves t_s values of $58/10/2\ \mu\text{s}$ from $1.84/10/50\text{ MHz}$ crystals. Yet it has a supply voltage of 1 V . Also, the ring oscillator entails frequency calibration after fabrication.

Dithering injection toggles the AO frequencies between two values by compensating the frequency deviation of the injection signal caused by temperature and voltage variations. As such, the injection signal can cover a wider frequency range than that of CFI. Still, trimming is necessary to compensate the process variation on the AO. Compared with CFI, its effect on shortening t_s is lower, since the signal power is spread to a wider spectrum. As a result, there is smaller power to be absorbed by the crystal at f_m . For instance, the XO in [6] exhibits a slashed t_s of $<400\ \mu\text{s}$ by using dithered-signal injection (dithered step size: 2%), but it still demands trimming to manage the process variations on the injection oscillator.

Here, we consider CI to be more robust and inexpensive, as it relies on a frequency-rich signal to excite the crystal and avoids frequency calibration. The principle is alike dithering but covers a wider frequency range. It gradually sweeps the oscillating frequency and progressively decreases/increases the frequency. As such, this chirping sequence can generate a spectrum between the highest frequency f_H and the lowest frequency f_L , as evinced by its Fourier transform [25]. If $f_L < f_m < f_H$ regardless of process, voltage, and temperature (PVT) variations, the power will be delivered to the crystal persistently. Despite its weaker effectiveness on t_s reduction since the power spreads to a wider band, CI has the benefit of no trimming on the AO. It is especially suitable for low-cost and ULV radios, where the frequency variation of the AO against voltage and temperature can be more exacerbated.

TABLE I
OVERVIEW OF DIFFERENT SIGNAL-INJECTION
TECHNIQUES TO KICK-START THE XO

	Characteristics of the injecting signal		
	Constant frequency	Dithering	Chirping
t_s & E_s reduction	✓✓✓	✓✓	✓
Trimming on AO	Required	Required	Not required
Precision of AO	Very critical	Critical	Relaxed
Literature	[14], [15]	[6]	[12] and this work

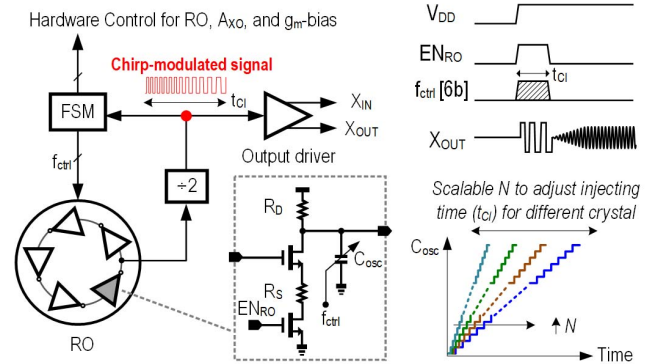


Fig. 5. Proposed SSCI. It generates a chirping signal to kick-start the XO using an untrimmed RO with relaxed precision. The FSM provides feasibility to scale t_{CI} , accommodating different crystal packages (i.e., L_M and C_S).

In [12], CI was applied together with the R_N -boosting technique, showing a t_s of $158\ \mu\text{s}$ without trimming or calibration on the AO. Still, the related RC -sweeping unit for modulating the frequency of the AO is area hungry (estimated $\sim 90\%$ of the chip area) due to its large time constant (at the order of $10\ \mu\text{s}$) for generating the chirping sequence. Table I summarizes the key features of the three signal-injection techniques.

To avoid the pitfalls of [12], we introduce the SSCI (Fig. 5) that only entails an untrimmed oscillator with relaxed precision. Its frequency range can easily cover f_m variation against PVT. Unlike the RC -based chirping [12], here we incorporate a five-stage RO with a finite state machine (FSM) to control the oscillating frequency of the RO via a cap-bank. Hence, the chirping sequence can be generated by referencing its own signal and requiring no area-hungry RC -units to modulate the oscillating frequency. The FSM counts the number of pulses and sequentially raises C_{OSC} by sending the control signal f_{ctrl} to the RO. In addition, compared to the analog sweeping technique in [12], the FSM can digitally scale the total injection time (t_{CI}), decided by the number of exciting cycles at each cap-bank value C_{OSC}

$$t_{CI} = N \times \sum_i t_i \quad (2)$$

where N is the number of cycles to repeat at each C_{OSC} , and t_i is the period of a single cycle at i th C_{OSC} . The average amplitude of oscillation on the crystal after the chirping sequence is proportional to $\sqrt{t_{CI}}$, as suggested from the Fourier transform of the chirping sequence [25] and also the time-domain

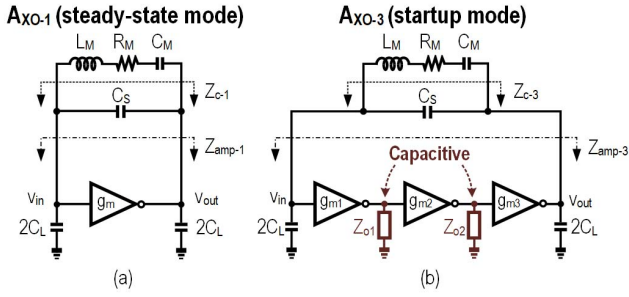


Fig. 6. XO using (a) one-single g_m (A_{XO-1}) for the steady-state and (b) three-stage g_m (A_{XO-3}) for the startup.

analysis in [12]. Thus, N can be programmed to adjust t_{CI} , rendering the XO easily compatible with different crystal parameters, i.e., an optimum t_{CI} depends on L_M , R_M and R_N (C_S) [12]. This digital-intensive architecture is more area efficient. The oscillation signal at the RO has varying duty-cycle with VT-variation. To maximize the injection energy (i.e., 50% duty cycle), the chirp-modulated signal is a div-by-2 output of the RO. This output serves as both the exciting signal for the crystal via the output driver, and the trigger signal for the FSM. The RO is powered down by the FSM automatically after the injection.

B. Dual-Mode g_m Scheme

The XO using a one-stage g_m (A_{XO-1}), especially for the Pierce oscillator, is popular as it can optimize the steady-state PN [6], [12]–[14], [26]. The g_m offers a negative resistance compensating the equivalent resistance of the crystal. Its value also determines the growth of the oscillation amplitude before the XO reaches the steady state. As shown in Fig. 6(a), by omitting the resistive loss induced by A_{XO-1} , the impedance between the I/O (Z_{amp-1}) becomes

$$Z_{amp-1} = -\frac{g_m}{4\omega_0^2 C_L^2} + \frac{1}{j\omega_0 C_L} \quad (3)$$

where C_L is the designated crystal's load capacitance and ω_0 is the angular oscillating frequency $2\pi f_0$. Since Z_{amp} is shunted by the crystal's stray capacitance (C_S), the negative resistance (R_N) of the overall impedance looking from the crystal core (Z_C) is affected

$$R_N \equiv -\text{Re}(Z_C) = \frac{-\text{Re}(Z_{amp})}{[\omega_0 C_S \text{Re}(Z_{amp})]^2 + [1 - \omega_0 C_S \text{Im}(Z_{amp})]^2}. \quad (4)$$

If $\omega_0 C_S |Z_{amp}| \ll 1$, we can have $R_N \approx -\text{Re}(Z_{amp})$ that matches the expression in [6] for A_{XO-1} . A large R_N favors more t_S reduction according to (1). Yet, for $|Z_{amp}|$ to be comparable with $1/\omega_0 C_S$ [i.e., a higher g_m and thus $|\text{Re}(Z_{amp})|$ to speed up the startup], we have to cogitate the effect from C_S . Thus, we can deduce the specific R_N of A_{XO-1} (i.e., $R_{N,1}$) from (4) as given by

$$R_{N,1} = \frac{4g_m C_L^2}{(g_m C_S)^2 + 16C_L^2 \omega_0^2 (C_L + C_S)^2}. \quad (5)$$

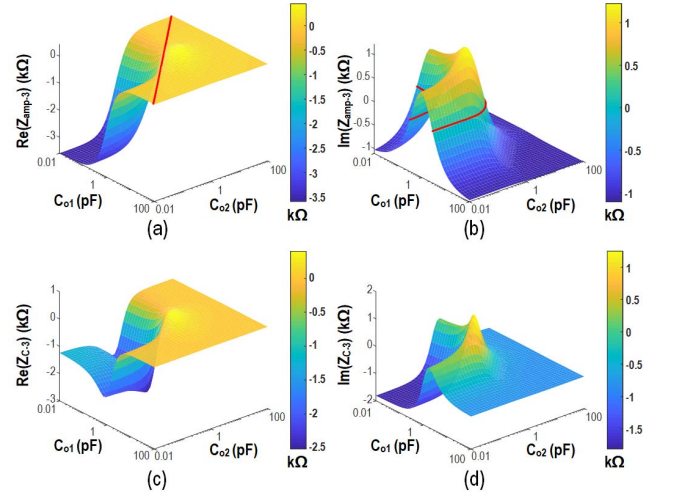


Fig. 7. Plot of the impedances as function of C_{o1} and C_{o2} . (a) $\text{Re}(Z_{amp-3})$. (b) $\text{Im}(Z_{amp-3})$. (c) $\text{Re}(Z_{C-3})$. (d) $\text{Im}(Z_{C-3})$. For (a) and (b), the contours where $\text{Re}(Z_{amp-3}) = 0$ k Ω and $\text{Im}(Z_{amp-3}) = 0$ k Ω are depicted with red lines.

Taking the derivative of (5), we can obtain the maximum value of $R_{N,1}$ with respect to g_m at a fixed C_L

$$R_{N,1,\max} = \frac{C_L}{2\omega_0 C_S (C_L + C_S)} \quad (6)$$

where we apply $g_m = 4\omega_0 C_L (1 + C_L/C_S)$. Obviously, $\text{Im}(Z_{amp-1})$ can only be negative (capacitive) for A_{XO-1} , and $R_{N,1}$ has an upper limit if only g_m is the sizing parameter [12], [13]. For instance, $R_{N,1}$ is limited to 1.2 k Ω with $C_S = 2$ pF, $f_0 = 24$ MHz, and $C_L = 6$ pF, even if we apply an oversized $g_m = 14.5$ mS. There were efforts to raise $R_{N,1}$ by increasing g_m or tuning C_L temporarily during the startup [13], [26], [27]. Yet, increasing g_m incurs in larger power consumption and is unfavorable toward reduction of E_S . Furthermore, $R_{N,1}$ is bound by (6), and is maximally $1/2\omega_0 C_S$ (i.e., 1.66 k Ω in the above example when $C_L \gg C_S$ and $g_m \approx 4\omega_0 C_L^2/C_S$).

Inspecting (4), if a positive $\text{Im}(Z_{amp})$ is possible to counteract the effect of C_S , R_N can be boosted to surmount the aforesaid R_N -limit. Our idea is to mimic a microhenry-range inductor on chip for this purpose. Interestingly, it is found that a three-stage g_m (A_{XO-3}) with designated capacitive loads (Z_{o1-2}) can effectively mimic an inductive effect during the startup [Fig. 6(b)]. Although a multistage g_m has been applied in [28] to save the XO's steady-state power, this paper explores first its inductive feature for t_S reduction. For A_{XO-3} , we define its Z_{amp} as Z_{amp-3} as given by

$$\begin{aligned} Z_{amp-3} &= \frac{-G_{m,\text{eff}}}{4\omega_0^2 C_L^2 (1 + j\omega_0 r_{o1} C_{o1})(1 + j\omega_0 r_{o2} C_{o2})} + \frac{1}{j\omega_0 C_L} \\ &= -\frac{G_{m,\text{eff}} (1 - \omega_0^2 r_{o1} C_{o1} r_{o2} C_{o2})}{4\omega_0^2 C_L^2 [1 + (\omega_0 r_{o1} C_{o1})^2][1 + (\omega_0 r_{o2} C_{o2})^2]} \\ &\quad + \frac{1}{j\omega_0 C_L} \left\{ 1 - \frac{G_{m,\text{eff}} (r_{o1} C_{o1} + r_{o2} C_{o2})}{4C_L [1 + (\omega_0 r_{o1} C_{o1})^2][1 + (\omega_0 r_{o2} C_{o2})^2]} \right\} \end{aligned} \quad (7)$$

where $G_{m,\text{eff}} = g_{m1} \cdot r_{o1} \cdot g_{m2} \cdot r_{o2} \cdot g_{m3}$ and $Z_{o1/2}$ is represented as a parallel load of $r_{o1/2}$ and $C_{o1/2}$. Since at 24 MHz the impedance of $2C_L$ at the output (553 Ω) is usually much smaller than the resistive load of the third stage, its resistive part is neglected. Manifested from (7), both the real and imaginary parts of $Z_{\text{amp-3}}$ are unbounded between positive and negative. For a positive $\text{Im}(Z_{\text{amp-3}})$, (8) has to be satisfied

$$\frac{G_{m,\text{eff}}(r_{o1}C_{o1} + r_{o2}C_{o2})}{[1 + (\omega_0 r_{o1} C_{o1})^2][1 + (\omega_0 r_{o2} C_{o2})^2]} > 4C_L. \quad (8)$$

Alternatively, for a negative $\text{Re}(Z_{\text{amp-3}})$, we set $1/(r_{o1,2}C_{o1,2}) > \omega_0$. In a practical design, the complete independent variables are only $C_{o1,2}$ and $g_{m1,2,3}$ as $r_{o1,2}$ are correlated with $g_{m1,2}$, especially when the voltage headroom is restrained. Fig. 7(a) and (b) plots $\text{Re}(Z_{\text{amp-3}})$ and $\text{Im}(Z_{\text{amp-3}})$, as a function of $C_{o1,2}$, respectively, where we set $g_{m1,2} = 0.4$ mS, $g_{m3} = 1.5$ mS, $r_{o1,2} = 7$ k Ω , $C_L = 6$ pF, and $\omega_0 = 2\pi \times 24$ MHz. At small $C_{o1,2}$, we have $\text{Re}(Z_{\text{amp-3}}) = -G_{m,\text{eff}}/4\omega_0^2 C_L^2$. $\text{Re}(Z_{\text{amp-3}})$ increases to 0 k Ω when we enlarge $C_{o1,2}$, and turn to positive if $C_{o1}C_{o2} > 1/\omega_0^2 r_{o1}r_{o2}$ [red line in Fig. 7(a)].

For $\text{Im}(Z_{\text{amp-3}})$, it is negative (capacitive) for sufficient small or large $C_{o1,2}$, but can be turned to positive (inductive) within a specific range, defined by the quadratic equation in (8) and shown in Fig. 7(b). By solving (8), the desired inductive effect can be achieved. For example, for $C_{o1} = C_{o2} = 0.5$ pF, the desirable inductive impedance $Z_{\text{amp-3}} = -1.6 + 1.2j$ k Ω can be achieved.

Fig. 7(c) and (d) shows the changes of $\text{Re}(Z_{C-3})$ and $\text{Im}(Z_{C-3})$ after paralleling A_{XO-3} , respectively, with $C_S = 2$ pF. When C_{o1} and C_{o2} are small, the value of $\text{Re}(Z_{C-3})$ (i.e., $-R_{N,3}$) is alike to that of A_{XO-1} and is bounded by (5), in which g_m is replaced by $G_{m,\text{eff}}$ that is ~ -1.2 k Ω . Such limitation can be surpassed here with an inductive $Z_{\text{amp-3}}$ as derived in Fig. 7(b). For instance, for $C_{o1} = C_{o2} = 0.5$ pF, we can have $\text{Re}(Z_{C-3}) = -2.4$ k Ω due to the inductive A_{XO-3} . Thus, a higher R_N can be achieved even with similar power consumption when compared to the A_{XO-1} , enabling an energy-efficient startup. Due to the intricate expression of $R_{N,3}$, its optimization is done numerically, as shown in Fig. 7(c), before proceeding to transistor-level implementation. Besides, our technique is also applicable to different f_0 . Using a similar mathematical model derived by (4) and (7) and changing the total g_m and $C_{o1,2}$ correspondingly, we have simulated to boost the R_N by $6.1\times$ at $f_0 = 10$ MHz and $7.4\times$ at $f_0 = 50$ MHz with the A_{XO-3} compared to A_{XO-1} . Since reference clock at 16/24 MHz is common for BLE as [6] and [13] reported, thus in this paper, we only focus on $f_0 = 16$ and 24 MHz.

Apparently, for the same power budget, A_{XO-3} is inferior to A_{XO-1} in terms of the steady-state PN, as each stage shares a smaller bias current and the noises accumulate. Also, for $\text{Im}(Z_{C-3})$ that determines the exact oscillating frequency of the XO, it deviates from the designated value due to the presence of C_{o1} and C_{o2} [Fig. 7(d)]. This affects the accuracy of f_0 . Thus, it is desirable to implement a dual-mode g_m scheme that can balance the startup and steady-state performances. During the startup where the PN and accuracy

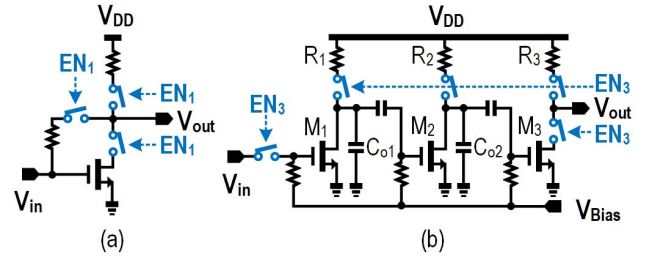


Fig. 8. Circuit implementation of (a) A_{XO-1} and (b) A_{XO-3} .

of f_0 are irrelevant, A_{XO-3} is enabled and connected to the crystal to attain a larger R_N for fast startup. When the crystal has gained sufficient energy for oscillation, A_{XO-3} is OFF and disconnected from the crystal while A_{XO-1} takes over to sustain the oscillation. As a result, the XO can benefit from both A_{XO-3} (fast startup) and A_{XO-1} (low PN and accurate f_0).

III. TRANSISTOR-LEVEL IMPLEMENTATION

The core elements of the XO (e.g., A_{XO-1} , A_{XO-3} , and RO) are designed to operate below a 0.5-V V_{DD} . Only the static and dc circuits (digital logic and constant- g_m bias circuit) operate at 0.7 V to facilitate the design. These circuits together consume <5 μA and are mostly powered-off during the steady state. Thus, the 0.7-V supply can be easily generated by an on-chip switched-capacitor charge pump and shared with other blocks at the system level as described in [22].

Both A_{XO-1} and A_{XO-3} are based on subthreshold common-source (CS) amplifiers with resistive loads [Fig. 8(a) and (b)]. Unlike other solutions that use current-source loads [6], [13], [14], the resistive load aids to preserve a moderate g_m even with $V_{DD} < 0.35$ V, for a small bias current (simulated at $I_{dc} = 100$ μA). For instance, the simulated g_m of A_{XO-1} is 1.3 mS at $V_{DD} = 0.3$ V and -40 $^\circ\text{C}$, being $4\times$ higher than that of the current-source load (assuming an identical g_m with $V_{DD} = 0.35$ V at 20 $^\circ\text{C}$). Furthermore, at high temperature, the intrinsic output resistance of the transistor decreases rapidly. This affects the stability of R_N and causes variation on t_s , especially for A_{XO-3} . The A_{XO-1} with resistive load has a tradeoff of lower immunity to power supply noise (noise power from V_{DD} modulated to the output of XO with a resistive load that is 3 dB larger than its current-source-load counterpart at 1-kHz offset). Also, it has a large f_0 variation since the g_m of A_{XO-1} is not fixed. Still, this is manageable for the BLE standard ($<\pm 50$ ppm [29]), as well as other IoT protocols (e.g., ZigBee: ± 40 ppm). A small nominal I_{dc} of 100 μA is adequate for the expected PN.

A_{XO-1} is self-biased by a feedback resistor R_F , whereas A_{XO-3} is an ac-coupled three-stage CS amplifier aided by a constant- g_m bias circuit. As revealed by (7), the g_m of the A_{XO-3} has a considerable impact on $R_{N,3}$. Thus, the constant- g_m bias circuit secures A_{XO-3} to be inductive, and a stable $R_{N,3}$ for robust-and-fast startup against PVT. The channel lengths of the transistors are chosen such that their output resistances are $\sim 10\times$ larger than the resistors R_{1-3} .

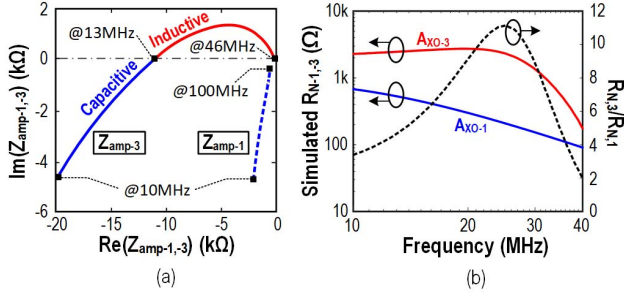


Fig. 9. (a) Locus plot of the $Z_{\text{amp-1,-3}}$ against frequency. (b) Simulated $R_{N,1}$ and $R_{N,3}$ with a fixed total g_m budget of 2.3 mS, and the boosting ratio against frequency.

This soothes temperature dependence of $R_{N,3}$ as r_{o1-3} are then dominated by R_{1-3} . On the other hand, the widths of the transistors are deterministic of the parasitic capacitances. Especially for C_{GS} of the transistor, it not only is sensitive to the operating conditions and affects $C_{o1,2}$ but also forms a capacitive divider with the ac-coupling network and degrades the gain; the gain attenuation should be controlled within 5% to depress their overall impacts. A_{XO-3} is designed to have similar power consumption ($\sim 100 \mu\text{A}$) as A_{XO-1} . As such, the power consumption does not vary instantaneously, easing the design and layout of the power supply. CMOS switches are inserted to each current branch such that A_{XO-1} or A_{XO-3} can be isolated from the crystal while lowering their leakage power (simulated $< 14 \text{ nW}$ at 0.35 V and 20 °C) when disabled. They have minimal channel lengths and adequate widths such that their ON-resistances are negligible when compared with R_{1-3} .

Both the parasitic capacitances of the transistors and the finite I/O resistance of A_{XO-3} will affect the accuracy of the derivation from (7). Thus, $R_{N,3}$ should be further optimized via simulation. The total g_m budget is 2.3 mS (total bias current: $100 \mu\text{A}$, assuming a $g_m/I_D = 23 \text{ V}^{-1}$), and r_{o1-3} are set according to the g_m of each gain stage. Fig. 9(a) shows the locus plots of $Z_{\text{amp-1}}$ and $Z_{\text{amp-3}}$ implemented with practical transistors and integrated passives. $Z_{\text{amp-1}}$ is capacitive over all frequencies, while $Z_{\text{amp-3}}$ is inductive over the 13-to-46-MHz range, rendering its compatible with different f_0 . Optimized at the most popular XO frequency of 24 MHz, the optimum $R_{N,3}$ is 2.4 k Ω after paralleling it with a C_S of 2 pF. This result is $\sim 9\times$ higher than $R_{N,1}$ under the same g_m budget and surpasses $R_{N,1,\text{max}}$ [Fig. 9(b)]. The boosting effect is insensitive to the frequency between 15 and 34 MHz, under $R_{N,3}/R_{N,1} > 6$.

The Monte-Carlo-simulated $R_{N,3}$ (mean) is $> 9.1\times$ higher than $R_{N,1}$, and the boosting factor is immune to $C_S = 1\text{--}3 \text{ pF}$, as specified from the crystal manufacturer (Fig. 10). We design $R_{N,1}$ to be $> 50 \Omega$ against PVT to compensate the resistive loss of the crystal (measured R_M of the crystal: 19 Ω), and safeguard the oscillation as well as PN of the XO.

Ideally, A_{XO-3} should be enabled for the entire startup phase. Yet the g_m values of M_{1-3} deviate from their small-signal values when the oscillation amplitude is growing. This results in an aggravated $R_{N,3}$. Thus, the optimum active time of $A_{XO-3}t_{\text{sw}}$ is the time when $R_{N,3} \approx R_{N,1}$, which means

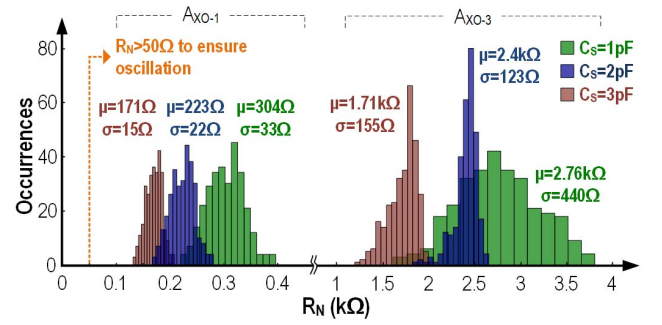


Fig. 10. Monte-Carlo-simulated R_N ($f_0 = 24 \text{ MHz}$, $N = 300$, $V_{\text{DD}} = 0.35 \text{ V}$).

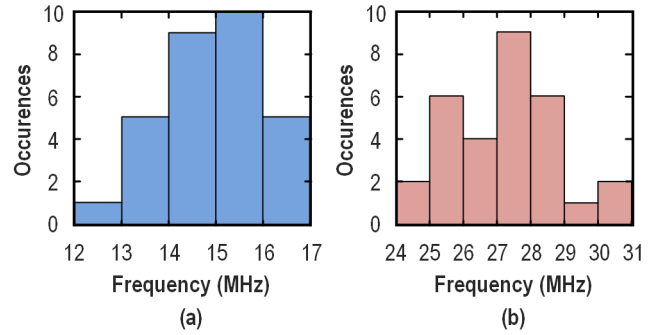


Fig. 11. (a) Monte-Carlo-simulated f_L with $V_{\text{DD}} = 0.4 \text{ V}$ and $T = 90 \text{ }^\circ\text{C}$. (b) Monte-Carlo-simulated f_H with $V_{\text{DD}} = 0.3 \text{ V}$ and $T = -40 \text{ }^\circ\text{C}$. $N = 30$ for both cases.

A_{XO-3} no longer helps t_s reduction. The optimal t_{sw} can be found via simulations with measured crystal parameters to avoid any extra detection and control mechanism.

To realize the SSCI, a five-stage RO is constituted by CS-amplifiers with source degeneration. Compared with the RO with inverters or relaxation oscillator, an RO with CS-amplifiers balances between the frequency stability and compatibility with the sub-0.5-V V_{DD} . The source resistor (R_S in Fig. 5) also reduces the variation of oscillating frequency against V_{DD} . From the simulation, the frequency variation of RO is reduced by $\sim 20\%$ over a 0.3-to-0.5 V V_{DD} . R_D is set to 36 k Ω . The current consumption of the RO is 20 μA . We implemented the div-by-2 unit and FSM with a standard logic.

We designed the f_H and f_L of the SSCI module as 36 and 12 MHz, respectively, which are chosen such that $f_L < f_m < f_H$ is satisfied even with PVT variation (Fig. 11). The total size of the C_{OSC} is simulated to be 135 fF to output an f_L of 12 MHz (after div-by-2). Then, the resolution of the cap-bank should be determined. This is decided by the minimum duration of t_{CI} ; since for a complete chirping sequence all of the states need to be swept at least once, the minimum t_{CI} (i.e., $N = 1$) is set by the resolution (number of pulses), as depicted in (2). The optimum t_{CI} , according to [12] and the measured crystal parameter, is derived as 4.6 μs . Thus, we set C_{OSC} as a binary-coded 6-bit cap-bank (unit cap: 2.14 fF), corresponding to a minimum t_{CI} of 4 μs with the designate

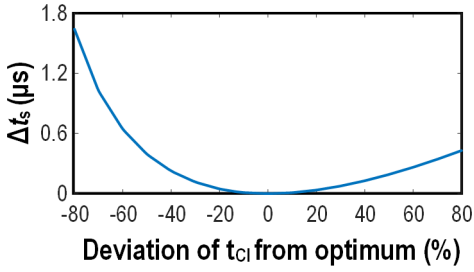


Fig. 12. Increase in t_s caused by the deviation of t_{CI} from the optimum duration.

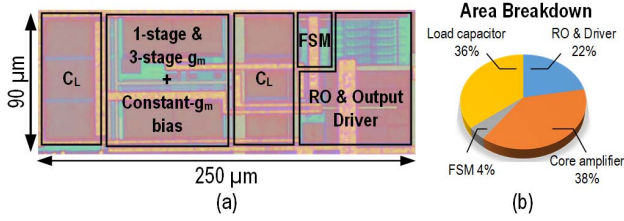


Fig. 13. (a) Chip micrograph. (b) Area breakdown of the XO.

f_H and f_L . Even though there is a discrepancy between the applied and optimum t_{CI} , the t_s is almost unaffected as the t_{CI} is only present for a short period when compared with t_s . As manifested in Section II-A, the amplitude of oscillation after the CI is proportional to $\sqrt{t_{CI}}$. Thus, even the applied t_{CI} is 13% shorter than the optimum in our case, the amplitude is only 7% smaller. Thanks to the high growth of the oscillation amplitude of the A_{XO-3} [time constant in (1): $9.33 \mu s$], the discrepancy between the applied and optimum t_{CI} can be compensated by the A_{XO-3} quickly, e.g., the $0.6 \mu s$ discrepancy is countervailed by the growth of oscillation amplitude in that $0.6 \mu s$ ($\sim 1.07\times$). No significant difference on t_s will emerge, even with PVT variation on the t_{CI} (Fig. 12).

The RO generates an oscillating signal at $2f_H$ with $C_{OSC} = 0$ fF (with oscillating frequency governed by the parasitic capacitances), and C_{OSC} is progressively increased by the FSM bit-by-bit according to N to $C_{OSC} = 135$ fF whereas the RO oscillates at $2f_L$. In this paper, the variable N is digitally configurable among 1, 2, 4, and 8.

IV. EXPERIMENTAL RESULTS

The XO was fabricated in 65-nm CMOS with fixed on-chip C_L of 6 pF. Extra cap-bank can be added to the XO for finer control of C_L if necessary. The active area is 0.023 mm^2 [Fig. 13(a)], of which 36% corresponds to the load capacitors [Fig. 13(b)]. The target f_0 can be flexible between 16 and 24 MHz. The FSM (i.e., t_{CI}) as well as the enabling of the V_{DD} are governed by a field-programmable-gate-array (Fig. 14). We first verify the SSCI functionality. Fig. 15(a) shows the measurement of the oscillating frequency of the RO (after div-by-2) against C_{OSC} , which is consistent with the post-layout simulation. The frequency range of the chirping sequence can safely cover the designated f_m against voltage and temperature variations. The average f_L and f_H across five dies at room

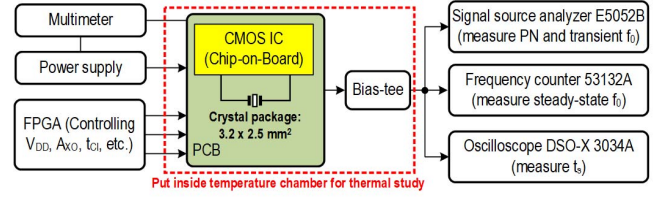


Fig. 14. Measurement setup of the XO.

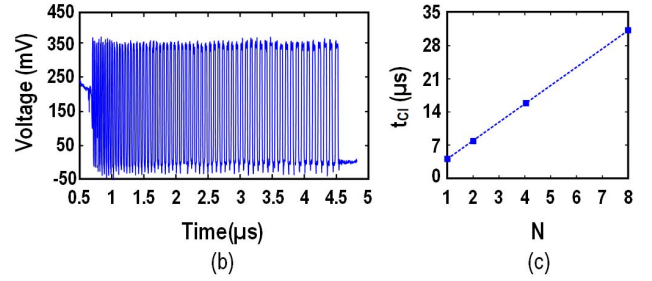
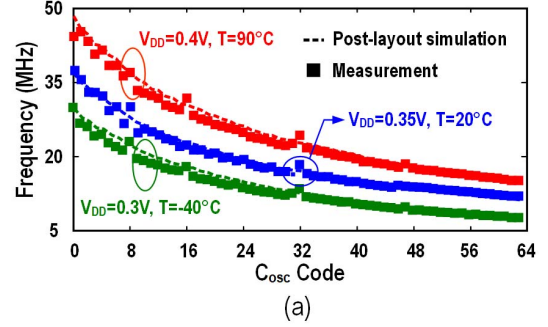


Fig. 15. (a) Measured and simulated oscillating frequencies of the RO versus C_{OSC} at different conditions, robust to cover f_0 of the crystal even with V_{DD} and temperature variations. (b) Measured chirping sequence ($N = 1$). (c) Injection duration t_{CI} against N . For the latter two figures, $V_{DD} = 0.35$ V, $T = 20^\circ \text{C}$.

temperature are 10.93 (σ : 0.32 MHz) and 35.96 MHz (σ : 1.21 MHz), respectively. Fig. 15(b) confirms the chirping sequence with $N = 1$ and Fig. 15(c) shows the duration of t_{CI} against N . This implies that the SSCI can generate a chirping sequence with variable t_{CI} ($4\text{--}32 \mu s$ in this paper) to accommodate different crystal parameters without resorting from area-hungry RC -units.

The XO was then tested with a 24-MHz crystal (package: $3.2 \times 2.5 \text{ mm}^2$) without any startup aid at room temperature (20°C) and $V_{DD} = 0.35$ V. The measured crystal parameters L_M , R_M , C_M , and C_S are 11.1 mH, 19Ω , 3.95 fF, and 1.3 pF, respectively. Under these conditions, we have $t_s = 1.3$ ms [Fig. 16(a)]. t_s is shortened to $530 \mu s$ when A_{XO-3} is enabled during the startup.

Since directly measuring R_N by inserting a resistance in series with the crystal is not viable (R_N is the real part of the impedance seen by the crystal core, which cannot be separated from the C_S), we have to estimate $R_{N,1}$ and $R_{N,3}$ from the growth of the oscillation amplitude according to (1), which can be rewritten as

$$\ln \left(\frac{A_{\text{env}}(t_0 + \Delta t)}{A_{\text{env}}(t_0)} \right) = \frac{R_N - R_M}{2L_M} \cdot \Delta t \quad (9)$$

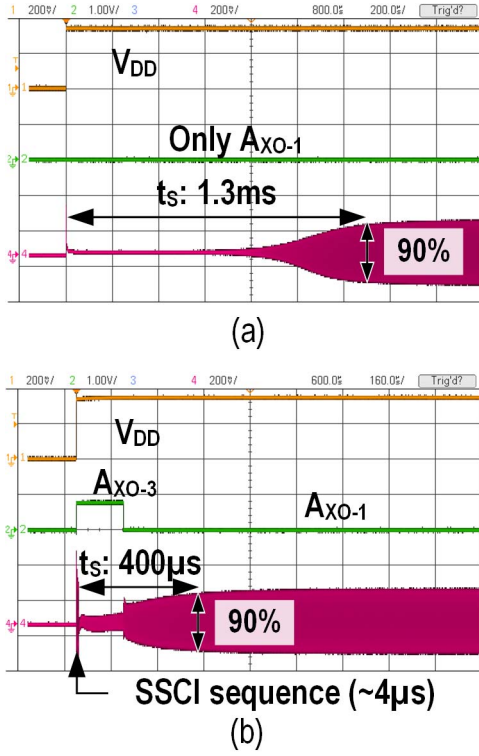


Fig. 16. Measured startup waveform (a) without startup aid and (b) with SSCI and A_{XO-3} enabled.

where t_0 is the starting time and Δt is the elapsed time. Hence, by measuring the growth of the oscillation amplitude within a specific time interval, the R_N of the XO can be estimated. For A_{XO-1} , the growth of oscillation is $1.01\times/\mu\text{s}$, and therefore $R_{N,1}$ is calculated as $230\ \Omega$ (Fig. 17), which is close to the prediction as described in Section III. Similarly, $R_{N,3} \approx 2.2\ \text{k}\Omega$ is found. The achieved R_N -boosting factor is $9.6\times$, coinciding with the simulation and evincing the functionality of A_{XO-3} .

Owing to two reasons, the reduction of t_s is not commensurate with the R_N -boosting ratio between A_{XO-3} and A_{XO-1} . First, as described in Section III, M_{1-3} will deviate from their nominal operating points and deteriorate $R_{N,3}$. This can be revealed by measuring t_s against t_{sw} (Fig. 18). When t_{sw} is short ($<60\ \mu\text{s}$) where M_{1-3} are in the subthreshold region, the small-signal model is still valid to estimate t_s against t_{sw} [i.e., slope of the curve (~ -10) closely matches with $-R_{N,3}/R_{N,1} + 1$]. As t_{sw} further increases, the oscillation drives M_{1-3} away from its original operating point and worsens $R_{N,3}$. Hence, the slope of the curve declines and eventually reaches zero whereas the A_{XO-3} no longer aids t_s -reduction. Second, the XO entails an overhead time to enter the steady state after switching to A_{XO-1} . After switching to A_{XO-1} , the XO still takes $\sim 380\ \mu\text{s}$ to enter the steady state. The improvement on t_s here is limited by the nonideality of the ULV A_{XO-3} . In fact, for the amplifiers with standard I/O voltage and higher output swing, the reduction of t_s should be more profound and better matched with the R_N -boosting ratio.

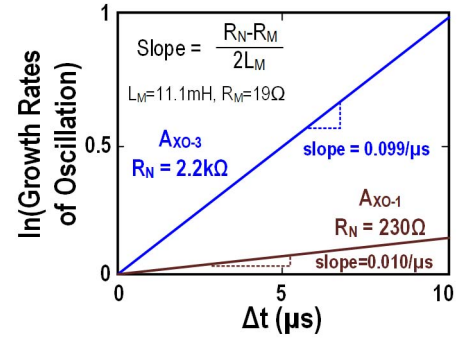


Fig. 17. Estimated R_N from the exponential growth of X_{OUT} 's amplitude (before the transistors enter triode/cutoff region).

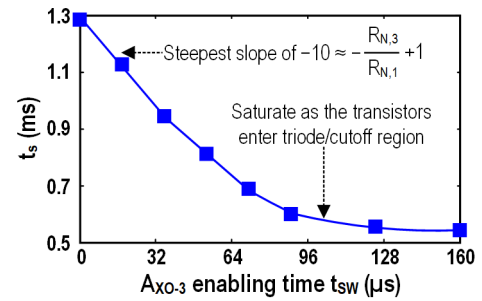


Fig. 18. Total t_s versus t_{sw} , the enabling time of A_{XO-3} (without SSCI).

With both A_{XO-3} and SSCI enabled, t_s is further shortened to $400\ \mu\text{s}$ ($3.3\times$ reduction) and the corresponding E_S is $14.2\ \text{nJ}$ ($2.8\times$ reduction) [Fig. 16(b)]. When switching from A_{XO-3} to A_{XO-1} that have different output impedances and thus operating frequency, there is an instantaneous change of the output swing, since the magnitude of current passing through the crystal does not change abruptly. The percentage of energy consumed in the startup phase by the SSCI, A_{XO-3} , and A_{XO-1} is 7% , 39% , and 53% , respectively. It has been verified that t_{sw} can tolerate $\pm 50\%$ uncertainty for $<10\%$ t_s variation, implying that an adequate t_s can be obtained even with non-optimal t_{sw} (e.g., variation on PVT and crystal's parameters). This also justifies that the existed RO will be good enough to control t_{sw} , avoiding any external detection and control mechanism.

For the transient frequency of the XO, it takes $\sim 300\ \mu\text{s}$ to settle for a $\pm 20\ \text{ppm}$ f_0 accuracy (i.e., $50\ \text{kHz}$ drifting from the center frequency of $2.44\ \text{GHz}$ in a packet, as defined in [29]). This result is $3.5\times$ faster than the case without startup aid (Fig. 19). Fig. 20 plots the summary of the reduction in t_s and E_S with different startup aids. The steady-state power is $31.8\ \mu\text{W}$ at $0.35\ \text{V}$, and the PN is $-134\ \text{dBc/Hz}$ at 1-kHz offset [Fig. 21(a)], being adequate for most IoT applications and comparable to other state-of-the-art XOs with a standard voltage (e.g., [4], it reports a PN of $-136\ \text{dBc/Hz}$ at $1\ \text{kHz}$ and at $f_0 = 26\ \text{MHz}$). As illustrated in Fig. 21(a), the PN of the A_{XO-1} is $15\ \text{dB}$ better than that of A_{XO-3} , confirming the poorer PN performance of the A_{XO-3} .

TABLE II
PERFORMANCE SUMMARY AND COMPARISON WITH RECENT ART

		This work		JSSC'16 [12]	ISSCC'16 [6]	ISSCC'17 [13]	JSSC'18 [14]†	
Applications		BLE		Bluetooth	BLE	BLE	N/A	
Fast-startup techniques		ULV inductive 3-stage g_m + SSCI		Chirp injection + g_m -boosting	Dithered injection	Dynamic load + g_m -boosting	Precisely-timed CFI	
Steady-state techniques		ULV 1-stage g_m + resistive load		1-stage inverter	1-stage g_m + current-source load			
CMOS process (nm)		65		180	65	90	65	
Active area (mm ²)		0.023		0.12	0.08	0.072	0.09 (per XO)	
Supply voltage, V_{DD} (V)		0.35*		1.5	1.68	1.0	1.0	
Temperature, T_{Range} (°C)		-40 to 90		-30 to 125	-40 to 90	-40 to 90	-40 to 85	
C_L (pF)		6		8 (off-chip)	6	9	10	9
Frequency, f_0 (MHz)		16	24	39.25	24	24	24	50
Startup energy, E_S (nJ)		15.8	14.2	349	--	--	36.7	13.3
Startup time, t_S (μ s)		460	400	158	64	435	200†	2.2
$\Delta t_S/t_S$ over T_{range}		9.8%	7.5%	7%	$\pm 35\%$	$\pm 20\%$	26.6%	7%
$\Delta f_0/f_0$ (ppm)	versus T_{Range}	21.9 \diamond	14.1 \diamond	± 5.5	N/A		N/A	
	versus V_{DD}	13.4 \S	17.9 \S	± 0.6 (1.2 to 1.8 V)	N/A		N/A	
Steady-state power (μ W)		31.6	31.8	181	393	693	95	195

* Digital & constant- g_m bias circuits are at 0.7 V (current budget: 5 μ A) to be generated by an on-chip charge pump as [22].

† Amplitude >90% and $\Delta f_0/f_0 < \pm 20$ ppm. \diamond @ 0.35 V. \S Across 0.3 to 0.5 V @ 20 °C.

‡ Only results from similar crystal packages were compared.

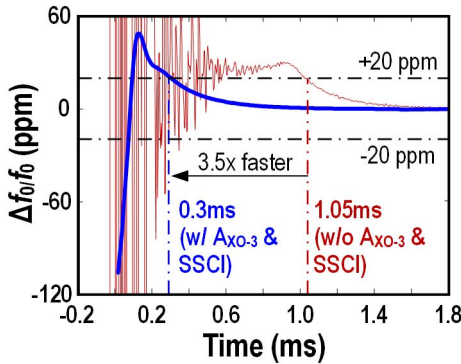


Fig. 19. Transient f_0 profiles of the XO ($V_{DD} = 0.35$ V, $T = 20$ °C).

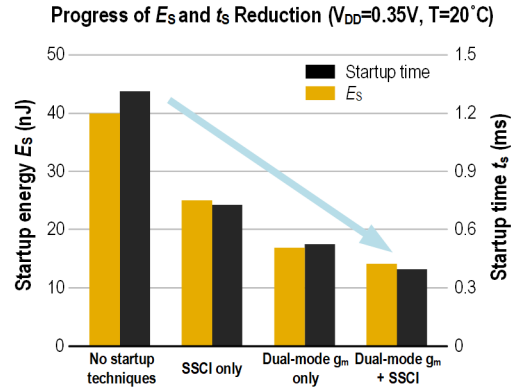


Fig. 20. Progress of E_S and t_S reduction of the XO ($f_0 = 24$ MHz) with different startup aids.

In terms of robustness, we confirm that the XO can uphold a steady-state output swing >80% of V_{DD} for $V_{DD} = 0.3$ – 0.5 V [Fig. 21(b)]. For the variation of t_S against V_{DD} , it is measured <25% from its mean (400 μ s) for $V_{DD} = 0.3$ – 0.5 V [Fig. 22(a)]. Only the RO of the SSCI fails to start if V_{DD} drops down to 0.25 V, but A_{XO-3} is still in place to aid t_S reduction. The frequency deviation ($\Delta f_0/f_0$) is 19.7 ppm (17.9 ppm) across 0.25 (0.3 V) to 0.5 V [Fig. 22(b)]. Over -40 °C– 90 °C, t_S variation is <7.5% [Fig. 22(c)], and the $\Delta f_0/f_0$ is 14.1 ppm [Fig. 22(d)]. Similar results were obtained for a 16-MHz crystal [i.e., $\Delta f_0/f_0 = 13.4$ ppm over 0.3–0.5 V, $\Delta f_0/f_0 = 21.9$ ppm over -40 °C– 90 °C, and t_S variation: 9.8%].

In another test, the XO was powered by a small commercial solar cell (1×3.8 cm²) in an indoor environment.

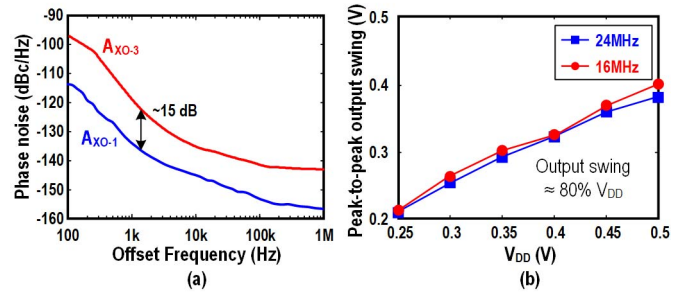


Fig. 21. (a) PN of the XO with A_{XO-1} and A_{XO-3} as core versus offset frequency ($f_0 = 24$ MHz). (b) Output voltage swing of the XO against V_{DD} .

Its nominal output voltage is close to 0.35 V at a solar irradiance of 0.4 mW/cm². Then, the output voltage of the solar cell is swept by altering the light reaching the solar cell.

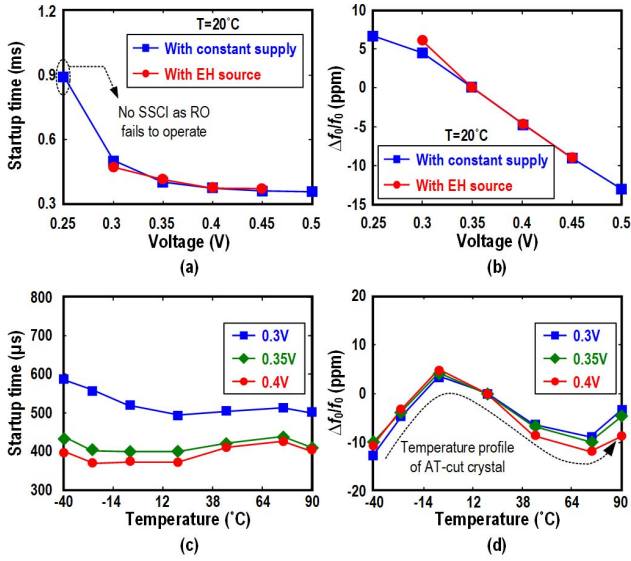


Fig. 22. Measured XO ($f_0 = 24$ MHz) performances. (a) Startup time against V_{DD} . (b) Frequency stability against V_{DD} . (c) Startup time against temperature. (d) Frequency stability against temperature.

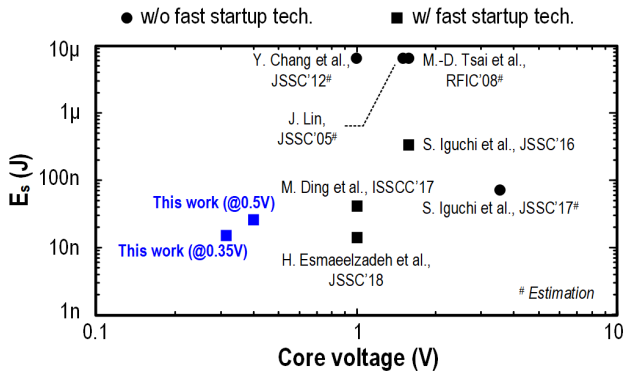


Fig. 23. Startup energy of XOs from the literature versus their core V_{DD} . Some of their E_s values (marked with #) were not reported, thus they are estimated through the multiplication of their startup times by the steady-state powers.

The measured metrics of the XO powered by the solar cell are comparable to those using a typical power supply [Fig. 22(a) and (b)].

Table II and Fig. 23 benchmark the performance of the XO with the prior art. In terms of E_s , this paper is $>2.6\times$ better than [13] and slightly higher than [14]. Furthermore, the proposed circuit can be considered in the vanguard, since it proves the feasibility of regulation-free operation under a wide range of sub-0.5-V V_{DD} , while conforming to the frequency-stability specification of the BLE standard.

V. CONCLUSION

A regulation-free sub-0.5-V XO for energy-harvesting BLE radios has been reported. Two circuit techniques, dual-mode g_m and SSCI, are introduced to reduce the startup time t_s and energy E_s . The dual-mode g_m exploits the inductive feature of a three-stage g_m (A_{XO-3}) to counteract C_S of the crystal during the startup, and the low-noise feature of a

one-stage g_m (A_{XO-1}) to preserve the PN in the steady state. Both A_{XO-1} and A_{XO-3} are ULV-enabled using resistive-load CS amplifiers. For the SSCI, a scalable chirping sequence effectively raises the initial oscillation amplitude of the crystal under different conditions, avoiding the need of a precisely trimmed AO. The XO prototyped in 65-nm CMOS has a compact area (0.023 mm^2) that is $>3.1\times$ smaller than the prior art. The measured t_s and E_s of the XO, with a 24-MHz crystal, are $400 \mu\text{s}$ and 14.2 nJ , respectively. The frequency stability against voltage (0.3–0.5 V) is 17.9 ppm and temperature ($-40 \text{ }^\circ\text{C}$ – $90 \text{ }^\circ\text{C}$) is 14.1 ppm; both conform to the BLE standard.

ACKNOWLEDGMENT

Part of the measurements was performed in Donhee Ham's Laboratory, Harvard University, Cambridge, MA, USA. The authors would like to thank the support offered there.

REFERENCES

- [1] A. Bahai, "Ultra-low energy systems: Analog to information," in *Proc. Eur. Solid-State Device Res. Conf.*, Oct. 2016, pp. 3–6.
- [2] J. Lin, "A low-phase-noise 0.004-ppm/step DCXO with guaranteed monotonicity in the 90-nm CMOS process," *IEEE J. Solid-State Circuits*, vol. 40, no. 12, pp. 2726–2734, Dec. 2005.
- [3] M.-D. Tsai, C.-W. Yeh, Y.-H. Cho, L.-W. Ke, P.-W. Chen, and G.-K. Dehng, "A temperature-compensated low-noise digitally-controlled crystal oscillator for multi-standard applications," in *Proc. IEEE Radio Freq. Integr. Circuits Symp. (RFIC)*, Jun. 2008, pp. 533–536.
- [4] Y. Chang, J. Leete, Z. Zhou, M. Vadipour, Y.-T. Chang, and H. Darabi, "A differential digitally controlled crystal oscillator with a 14-bit tuning resolution and sine wave outputs for cellular applications," *IEEE J. Solid-State Circuits*, vol. 47, no. 2, pp. 421–434, Feb. 2012.
- [5] S. Iguchi, T. Sakurai, and M. Takamiya, "A low-power CMOS crystal oscillator using a stacked-amplifier architecture," *IEEE J. Solid-State Circuits*, vol. 52, no. 11, pp. 3006–3017, Nov. 2017.
- [6] D. Griffith, J. Murdock, and P. T. Røine, "A 24 MHz crystal oscillator with robust fast start-up using dithered injection," in *IEEE Int. Solid-State Circuits Conf. (ISSCC) Dig. Tech. Papers*, Jan./Feb. 2016, pp. 104–105.
- [7] Nordic Semiconductor. (2018). *nRF52840 Data Sheet*. [Online]. Available: http://infocenter.nordicsemi.com/pdf/nRF52840_PS_v1.0.pdf
- [8] Y.-H. Liu *et al.*, "A 3.7 mW-RX 4.4 mW-TX fully integrated Bluetooth Low-Energy/IEEE802.15.4/proprietary SoC with an ADPLL-based fast frequency offset compensation in 40 nm CMOS," in *IEEE Int. Solid-State Circuits Conf. (ISSCC) Dig. Tech. Papers*, Feb. 2015, pp. 236–237.
- [9] F.-W. Kuo *et al.*, "A Bluetooth low-energy transceiver with 3.7-mW all-digital transmitter, 2.75-mW high-IF discrete-time receiver, and TX/RX switchable on-chip matching network," *IEEE J. Solid-State Circuits*, vol. 52, no. 4, pp. 1144–1162, Apr. 2017.
- [10] H. Liu *et al.*, "An ADPLL-centric Bluetooth low-energy transceiver with 2.3 mW interference-tolerant hybrid-loop receiver and 2.9 mW single-point polar transmitter in 65 nm CMOS," in *IEEE Int. Solid-State Circuits Conf. (ISSCC) Dig. Tech. Papers*, Feb. 2018, pp. 444–445.
- [11] S. A. Blanchard, "Quick start crystal oscillator circuit," in *Proc. IEEE Univ./Govt./Ind. Microelectron. Symp.*, Jul. 2003, pp. 78–81.
- [12] S. Iguchi, H. Fuketa, T. Sakurai, and M. Takamiya, "Variation-tolerant quick-start-up CMOS crystal oscillator with chirp injection and negative resistance booster," *IEEE J. Solid-State Circuits*, vol. 51, no. 2, pp. 496–508, Feb. 2016.
- [13] M. Ding *et al.*, "A 95 μW 24 MHz digitally controlled crystal oscillator for IoT applications with 36 nJ start-up energy and $>13\times$ start-up time reduction using a fully-autonomous dynamically-adjusted load," in *IEEE Int. Solid-State Circuits Conf. (ISSCC) Dig. Tech. Papers*, Feb. 2017, pp. 90–91.
- [14] H. Esmaeizadeh and S. Pamarti, "A quick startup technique for high- Q oscillators using precisely timed energy injection," *IEEE J. Solid-State Circuits*, vol. 53, no. 3, pp. 692–702, Mar. 2018.

- [15] Y. I. Kwon, S.-G. Park, T.-J. Park, K.-S. Cho, and H.-Y. Lee, "An ultra low-power CMOS transceiver using various low-power techniques for LR-WPAN applications," *IEEE Trans. Circuits Syst. I, Reg. Papers*, vol. 59, no. 2, pp. 324–336, Feb. 2012.
- [16] Texas Instruments. (2013). *CC2541 Data Sheet*. [Online]. Available: <http://www.ti.com/lit/ds/symlink/cc2541.pdf>
- [17] S. Bandyopadhyay and A. P. Chandrakasan, "Platform architecture for solar, thermal, and vibration energy combining with MPPT and single inductor," *IEEE J. Solid-State Circuits*, vol. 47, no. 9, pp. 2199–2215, Sep. 2012.
- [18] P.-S. Weng, H.-Y. Tang, P.-C. Ku, and L.-H. Lu, "50 mV-input batteryless boost converter for thermal energy harvesting," *IEEE J. Solid-State Circuits*, vol. 48, no. 4, pp. 1031–1041, Apr. 2013.
- [19] J. Bito, R. Bahr, J. G. Hester, S. A. Nauroze, A. Georgiadis, and M. M. Tentzeris, "A novel solar and electromagnetic energy harvesting system with a 3-D printed package for energy efficient Internet-of-Things wireless sensors," *IEEE Trans. Microw. Theory Techn.*, vol. 65, no. 5, pp. 1831–1842, May 2017.
- [20] F. Zhang, Y. Miyahara, and B. P. Otis, "Design of a 300-mV 2.4-GHz receiver using transformer-coupled techniques," *IEEE J. Solid-State Circuits*, vol. 48, no. 12, pp. 3190–3205, Dec. 2013.
- [21] M. Babaie *et al.*, "A fully integrated Bluetooth low-energy transmitter in 28 nm CMOS With 36% system efficiency at 3 dBm," *IEEE J. Solid-State Circuits*, vol. 51, no. 7, pp. 1547–1565, Jul. 2016.
- [22] W.-H. Yu, H. Yi, P.-I. Mak, J. Yin, and R. P. Martins, "A 0.18 V 382 μ W Bluetooth low-energy (BLE) receiver with 1.33 nW sleep power for energy-harvesting applications in 28 nm CMOS," in *IEEE Int. Solid-State Circuits Conf. (ISSCC) Dig. Tech. Papers*, Feb. 2017, pp. 414–415.
- [23] J. Yin, S. Yang, H. Yi, W.-H. Yu, P.-I. Mak, and R. P. Martins, "A 0.2 V energy-harvesting BLE transmitter with a micropower manager achieving 25% system efficiency at 0 dBm output and 5.2 nW sleep power in 28 nm CMOS," in *IEEE Int. Solid-State Circuits Conf. (ISSCC) Dig. Tech. Papers*, Feb. 2018, pp. 450–451.
- [24] K.-M. Lei, P.-I. Mak, M.-K. Law, and R. P. Martins, "A regulation-free sub-0.5 V 16/24 MHz crystal oscillator for energy-harvesting BLE radios with 14.2 nJ startup energy and 31.8 μ W steady-state power," in *IEEE Int. Solid-State Circuits Conf. (ISSCC) Dig. Tech. Papers*, Feb. 2018, pp. 52–53.
- [25] J. R. Klauder, A. C. Price, S. Darlington, and W. J. Albersheim, "The theory and design of chirp radars," *Bell Syst. Tech. J.*, vol. 39, no. 4, pp. 745–808, 1960.
- [26] E. A. Vittoz, M. G. R. Degrauwe, and S. Bitz, "High-performance crystal oscillator circuits: Theory and application," *IEEE J. Solid-State Circuits*, vol. JSSC-23, no. 3, pp. 774–783, Jun. 1988.
- [27] K.-M. Lei, P.-I. Mak, and R. P. Martins, "A 0.4 V 4.8 μ W 16 MHz CMOS crystal oscillator achieving 74-fold startup-time reduction using momentary detuning," in *Proc. IEEE Int. Symp. Circuits Syst. (ISCAS)*, May 2017, pp. 2791–2794.
- [28] S. Iguchi, A. Saito, Y. Zheng, K. Watanabe, T. Sakurai, and M. Takamiya, "93% power reduction by automatic self power gating (ASPG) and multistage inverter for negative resistance (MINR) in 0.7 V, 9.2 μ W, 39 MHz crystal oscillator," in *IEEE Symp. VLSI Circuits Dig. Tech. Papers*, Jun. 2013, pp. C142–C143.
- [29] *Bluetooth Core Specification V5.0*. Accessed: Jan. 1, 2017. [Online]. Available: <https://www.bluetooth.com/specifications/bluetooth-core-specification>



Ka-Meng Lei (S'12–M'17) received the B.Sc. degree in electrical and electronics engineering from Honours College, University of Macau, Macau, China, in 2012, and the Ph.D. degree in electrical and computer engineering from the State-Key Laboratory of Analog and Mixed-Signal VLSI, Faculty of Science and Technology, University of Macau, in 2016.

He serves as a Lecturer under the UM Macao Fellow Program with the University of Macau. He serves as a Post-Doctoral Fellow (visiting) with

Donhee Ham's Laboratory, where he is involved in high-resolution portable nuclear magnetic resonance (NMR) spectroscopy. He has co-authored one book *Handheld Total Chemical and Biological Analysis Systems: Bridging NMR, Digital Microfluidics, and Semiconductors* (Springer, 2018) and one book chapter *Micro-NMR on CMOS for Biomolecular Sensing* (Springer, 2018). He has also authored or co-authored 16 referred papers, seven in scientific journals, and nine in conference proceedings. His current research interests include ultralow voltage analog circuit techniques, sensors and analog front-end interfaces, high-resolution portable NMR platform, and system planning, integration, and optimization for biomedical devices.

Dr. Lei was a (co-)recipient of the Chipidea Microelectronics Prize 2012 (undergraduate) and 2017 (postgraduate), the Best Paper Award in ASQED 2013, the Student/Young Researcher Grant from The Chemical and Biological Microsystems Society 2015, the Distinguished Design Award from the IEEE A-SSCC 2015, the Silkroad Award from the ISSCC 2016, the FDCT Macao Science and Technology Award for Postgraduates 2016 (Ph.D. level), the 2016 Young Researcher Award from the Instituto Internacional de Macau, and the IEEE SSCS Predoctoral Achievement Award in 2017. He is a Reviewer for several scientific journals and conferences, including the IEEE TRANSACTIONS ON BIOMEDICAL CIRCUITS AND SYSTEMS and the IEEE SENSORS JOURNAL.



Pui-In Mak (S'00–M'08–SM'11) received the Ph.D. degree from the University of Macau (UM), Macau, China, in 2006.

He is currently a Full Professor with the Department of Electronic and Computer Engineering, Faculty of Science and Technology, UM, and an Associate Director (Research) with the State Key Laboratory of Analog and Mixed-Signal VLSI, UM. His current research interests include analog and radio frequency circuits and systems for wireless and multidisciplinary innovations.

Dr. Mak was an Editorial Board Member of the IEEE Press from 2014 to 2016 and a member of the Board-of-Governors of the IEEE Circuits and Systems Society from 2009 to 2011. He has been a TPC Member of ISSCC since 2016. He was a (co-)recipient of the DAC/ISSCC Student Paper Award in 2005, the CASS Outstanding Young Author Award in 2010, the National Scientific and Technological Progress Award in 2011, the Best Associate Editor of the IEEE TRANSACTIONS ON CIRCUITS AND SYSTEMS II from 2012 to 2013, the A-SSCC Distinguished Design Award in 2015, and the ISSCC Silkroad Award in 2016. In 2005, he was decorated with the Honorary Title of Value for scientific merits by the Macau Government. He was the TPC Vice Co-Chair of ASP-DAC in 2016, a TPC Member of A-SSCC from 2013 to 2016, and ESSCIRC from 2016 to 2017. He is currently the Chair of the Distinguished Lecturer Program of the IEEE Circuits and Systems Society. He was a Senior Editor of the IEEE JOURNAL ON EMERGING AND SELECTED TOPICS IN CIRCUITS AND SYSTEMS from 2014 to 2015 and an Associate Editor of the IEEE TRANSACTIONS ON CIRCUITS AND SYSTEMS I from 2010 to 2011 and 2014 to 2015 and the IEEE TRANSACTIONS ON CIRCUITS AND SYSTEMS II from 2010 to 2013. He has been an Associate Editor of the IEEE SOLID-STATE CIRCUITS LETTERS since 2017 and the IEEE JOURNAL OF SOLID-STATE CIRCUITS since 2018. He is/was a Distinguished Lecturer of the IEEE Circuits and Systems Society from 2014 to 2015 and the IEEE Solid-State Circuits Society during 2017–2018.



Man-Kay Law (M'11–SM'16) received the B.Sc. degree in computer engineering and the Ph.D. degree in electronic and computer engineering from The Hong Kong University of Science and Technology (HKUST), Hong Kong, in 2006 and 2011, respectively.

Since 2011, he has been with HKUST as a Visiting Assistant Professor. He is currently an Associate Professor with the State Key Laboratory of Analog and Mixed-Signal VLSI, Faculty of Science and Technology, University of Macau, Macau, China. He

was with the Zhejiang Advanced Manufacturing Institute and HKUST, where he was developed an ultralow power fully integrated CMOS temperature sensing passive UHF RFID tag together. He has authored or co-authored over 70 technical journals and conference papers and holds six U.S. patents. His current research interests include the development of ultralow power sensing circuits and integrated energy harvesting techniques for wireless and biomedical applications.

Dr. Law was a member of the Technical Program Committee of the Asia Symposium on Quality Electronic Design from 2012 to 2013, and a Review Committee Member of the IEEE International Symposium on Circuits and Systems from 2012 to 2015, the Biomedical Circuits and Systems Conference from 2012 to 2015, the International Symposium on Integrated Circuits in 2014, and the University Design Contest Co-Chair of Asia and South Pacific Design Automation Conference in 2016. He serves as a Technical Committee Member of the IEEE CAS Committees on Sensory Systems and the IEEE CAS Committee on Biomedical Circuits and Systems. He is also an ITPC Member of the IEEE International Solid-State Circuits Conference. He was a co-recipient of the ASQED Best Paper Award in 2013, the A-SSCC Distinguished Design Award in 2015, and the ASPDAC Best Design Award in 2016. He received the Macao Science and Technology Invention Award (Second Class) by the Macau Government—FDCT in 2014.



Rui P. Martins (M'88–SM'99–F'08) was born in 1957. He received the bachelor's, master's, Ph.D., and Habilitation degrees in electrical engineering and computers from the Department of Electrical and Computer Engineering, Instituto Superior Técnico (IST), University of Lisbon, Lisbon, Portugal, in 1980, 1985, 1992, and 2001, respectively.

Since 1980, he has been with the Department of Electrical and Computer Engineering, IST, University of Lisbon. Since 1992, he has been with the, Department of Electrical and Computer Engineering,

Faculty of Science and Technology (FST), University of Macau (UM), Macao, China, where he was the Dean of the faculty from 1994 to 1997, and has been a Chair-Professor since 2013 and the Vice-Rector since 1997. Within the scope of his teaching and research activities, he has taught 21 bachelor's and master's courses, and, in UM, has supervised (or co-supervised) 45 theses, the Ph.D. (24) and master's (21) theses. He was the Co-Founder of Synopsys from 2001 to 2002, and the Founding Director of the Analog and Mixed-Signal VLSI Research Laboratory, UM, and the State Key Laboratory of China (the first in Engineering in Macau), being its. He has co-authored seven books and 11 book chapters, and 442 papers, 141 papers in scientific journals, and 301 papers in conference proceedings, and other 64 academic works. He holds 28 U.S. patents and two Taiwan patents.

Dr. Martins was elected, unanimously, as a Corresponding Member of the Portuguese Academy of Sciences (in Lisbon), being the only Portuguese

Academician living in Asia in 2010. He was a Nominations Committee Member of the IEEE CASS from 2016 to 2017. He has been a member of the IEEE CASS Fellow Evaluation Committee since 2013, and CAS Society representative in the Nominating Committee, for the election in 2014, of the Division I (CASS/EDS/SSCS)—the Director of the IEEE. He was a recipient of two government decorations, including the Medal of Professional Merit from Macao Government (Portuguese Administration) in 1999 and the Honorary Title of Value from Macao SAR Government (Chinese Administration) in 2001. He received the IEEE Council on Electronic Design Automation Outstanding Service Award in 2016. He was nominated as the Best Associate Editor of T-CAS II from 2012 to 2013. He was the Founding Chairman of the IEEE Macau Section from 2003 to 2005 and the IEEE Macau Joint-Chapter on Circuits And Systems (CAS)/Communications(COM) from 2005 to 2008 [2009 *World Chapter of the Year of IEEE CAS Society (CASS)*]. He was the General Chair of 2008 the IEEE Asia-Pacific Conference on CAS—APCCAS'2008 and the Vice-President for Region 10 (Asia, Australia, and the Pacific) of the IEEE CASS from 2009 to 2011. He was the General Chair of the ACM/IEEE Asia South Pacific Design Automation Conference—ASP-DAC'2016 and. He the Chair of the IEEE CASS Fellow Evaluation Committee (Class 2018). He was the Vice-President from 2005 to 2014) and the President of the Association of Portuguese Speaking Universities from 2014 to 2017. He was the Vice-President (World) Regional Activities and Membership of the IEEE CASS from 2012 to 2013. He was an Associate Editor of the IEEE TRANSACTIONS ON CAS II: EXPRESS BRIEFS from 2010 to 2013.